ADVANCED FUNCTIONAL MATERIALS
www.afm-journal.de

Dynamically Controllable Terahertz Electromagnetic Interference Shielding by Small Polaron Responses in Dirac Semimetal $PdTe_2$ Thin Films

Yingyu Guo, Zhongqiang Chen, Zuanming Jin, Xuefeng Wang,* Chao Zhang, Alexey V. Balakin, Alexander P. Shkurinov, Yan Peng,* Yiming Zhu,* and Songlin Zhuang*

Terahertz (THz) electromagnetic interference (EMI) shielding materials is crucial for ensuring THz electromagnetic protection and information confidentiality technology. Here, it is demonstrated that high electrical conductivity and strong absorption of THz electromagnetic radiation by type-II Dirac semimetal $PdTe_2$ film make it a promising material for EMI shielding. Compared to MXene film, a commonly used metallic 2D material, the $PdTe_2$ film demonstrates a remarkable 40.36% increase in average EMI shielding efficiency per unit thickness within a broadband THz frequency range. Furthermore, it is demonstrated that a photoinduced long life-time THz transparency in Dirac semimetal $PdTe_2$ films is attributed to the formation of small polarons due to the strong electron-phonon coupling. A 15 nm-thick $PdTe_2$ film exhibits a photoinduced change of EMI SE of 1.1 dB, a value exceeding three times that measured on MXene film with a similar pump fluence. This work provides insights into the fundamental photocarrier properties in type-II Dirac semimetals that are essential for designing advanced THz optoelectronic devices.

1. Introduction

The Terahertz (THz) radiation is located between the realms of electronics and photonics.[1–4] THz science and technology rapidly develop in biomedical imaging, sensing, and spectroscopy, beyond 5G wireless communication and intelligent electronics.[5–8] Electromagnetic security risks in the terahertz frequency range, such as electromagnetic radiation, interference, and information stealing, are worth raising serious concerns about. In addition, electromagnetic interference (EMI) greatly increases the possibility of system disruption and device damage.[9–11] Many metallic thin film materials, such as metal foils, carbon-based materials, graphene materials have been used for THz wave electromagnetic shielding.[12–29] However, the efficiency and bandwidth of EMI shielding for these materials are relatively limited, as shown in **Table 1**. In addition, the EMI shielding cannot be actively controlled. Therefore, new materials and strategies are required to address these challenges.

Over the last two decades, 2D transition metal dichalcogenides (TMDs) have shown great application potential in numerous fields, such as optics, electronics, and optoelectronics.[30–32] TMDs with a chemical stoichiometry of MX_2, where M stands for a transition metal from groups

Y. Guo, Z. Jin, Y. Peng, Y. Zhu, S. Zhuang
Terahertz Technology Innovation Research Institute
Terahertz Spectrum and Imaging Technology Cooperative Innovation Center
Shanghai Key Lab of Modern Optical System
University of Shanghai for Science and Technology
Shanghai 200093, China
E-mail: physics_jzm@usst.edu.cn; py@usst.edu.cn; ymzhu@usst.edu.cn

Z. Chen, X. Wang
Jiangsu Provincial Key Laboratory of Advanced Photonic and Electronic Materials
School of Electronic Science and Engineering
Collaborative Innovation Center of Advanced Microstructures
Nanjing University
Nanjing 210093, China
E-mail: xfwang@nju.edu.cn

Z. Jin, Y. Peng, Y. Zhu, S. Zhuang
Shanghai Institute of Intelligent Science and Technology
Tongji University
Shanghai 200092, China

C. Zhang
School of Physics
University of Wollongong
Wollongong, New South Wales 2522, Australia

A. V. Balakin, A. P. Shkurinov
Department of Physics and International Laser Center
Lomonosov Moscow State University
LeninskieGory 1, Moscow 19991, Russia

A. V. Balakin, A. P. Shkurinov
ILIT RAS-Branch of the FSRC ⟪Crystallography and Photonics⟫ RAS
Svyatoozerskaya 1, Shatura, Moscow Region 140700, Russia

The ORCID identification number(s) for the author(s) of this article can be found under https://doi.org/10.1002/adfm.202407749

DOI: 10.1002/adfm.202407749

Table 1. Comparison of THz EMI shielding performance for various materials.

	Material	Thickness [μm]	EMI SE [dB]	Specific SE [dB μm^{-1}]	Frequency Range [THz]	Refs.
MXene-based	$Ti_3C_2T_y$ film	0.025	2.5	100	0.25–2.25	[12]
	Zn+ MXene foam	85	51	0.63	0.2–2.0	[13]
	MXene waterborne paint	38.3	64.9	1.69	0.2–1.6	[14]
	MXene/polyaramid	20	52.7	2.635	0.2–1.6	[15]
	polyimide-2D MXene	110	70.4	0.64	0.1–2.0	[16]
	MXene/rGO film	148	54.2	0.366	0.37–2.0	[17]
	polypyrrole/$Ti_3C_2T_x$	4	71.4	17.85	0.2–1.6	[18]
	Wrinkled MXene	0.008	5.6	700	0.2–10.0	[19]
Graphene-based	Graphene foam	3000	74	0.025	0.1–1.6	[20]
	Cu/graphene	0.160	60.95	380.9	0.1–1.0	[21]
	graphene/PMMA	33	60	1.82	0.2–2.0	[22]
	Polyvinyl alcohol/GO/Ag	114	8	0.070	0.5–2.5	[23]
Carbon-based	Kapton-derived Carbon	125	65	0.52	0.22–0.5	[24]
	Graphitic carbon microspheres	3.75	27.5	7.33	0.1–1.6	[25]
	carbon nanofibers/Nylon 6,6	570	44	0.077	0.2–1.2	[26]
Metal	Ag nanocrystals	1.3	60	48	0.0082–0.0124	[27]
	Al foil	8	66	8.25	0.0082–0.0124	[28]
	Cu mesh	2.5	40.4	16.0	0.0082–0.0124	[29]
	Cu foil	0.04	44.55	1113.75	0.1–1.0	[21]
Dirac semimetals	$PdTe_2$	0.015	14.00 ± 2.93	933.33 ± 195.33	0.2–2.0	This work
	$PdTe_2$	0.020	19.65 ± 4.80	982.50 ± 240.00	0.2–2.0	

IV-VII (Mo, Pt or Pd) and X is chalcogen elements (S, Se, or Te), form a well-known class of layered van der Waals materials.[33–35] Palladium ditelluride ($PdTe_2$) has been known as a type II Dirac semimetal,[36,37] which has gained increasing attention due to superconductivity,[38–41] low effective mass,[42] ultrahigh carrier mobility[43] and strong electron-phonon (*e*-ph) coupling.[44,45] In addition, $PdTe_2$ shows planar Hall effect,[46] high thermoelectricity,[47–49] and nonlinear optical properties.[50] These have demonstrated the potential applications of $PdTe_2$ in saturable absorbers,[50,51] photocatalysis,[52] and THz photodetectors.[53–56]

Based on Schelkunof's theory, the EMI shielding efficiency (EMI SE) is related to the conductivity of thin films.[57] $PdTe_2$ thin films exhibit excellent electrical conductivity in the range of 10^6–10^7 S m^{-1}, which is higher than most TMDs and is comparable to some conventional metals, suggesting its great potential as contact materials,[58–61] THz absorbers[62] and EMI shielding materials.[63–66] THz time-domain spectroscopy (THz-TDS) is one of the preferred methods for investigating the intrinsic carrier transport of materials and their applications in the THz frequency range. The interaction of THz light with type II Dirac semimetal can not only gain new important scientific insights into how these materials behave, but also possibilities of new devices and applications.[67–73]

In this letter, we demonstrate that topological semimetal $PdTe_2$ can be used as an efficient material for THz EMI shielding. THz time-domain spectroscopy is used to demonstrate the high conductivity of $PdTe_2$ in THz frequency range experimentally. The real and imaginary parts of the THz conductivity of $PdTe_2$ thin films were fitted by the Drude-Smith (DS) model, which determines the key optoelectronic parameters, such as electron density, electronic localization factor, and electron relaxation time. We demonstrate that the highly conductive $PdTe_2$ semimetal thin film has significant THz EMI shielding properties, which scales with the film thickness, and can reach as high as ≈ 24.28 dB at 1.78 THz for a 20-nm-thick $PdTe_2$ film, corresponding to the specific EMI SE per unit thickness of 1214.00 dB μm^{-1}. Importantly, we use a time-resolved THz spectroscopy to investigate the photoinduced ultrafast carrier dynamics of $PdTe_2$ thin films at room temperature. The photoexcitation by an optical pulse (1.55 eV) results in a negative conductivity in $PdTe_2$ for hundreds of picoseconds. The long relaxation bleaching THz electromagnetic interference shielding is attributed to the formation of small polarons due to the strong electron-phonon coupling, which is confirmed by pump-fluence and film-thickness dependent measurements. This behavior can be used to control over the THz EMI shielding dynamically, extending a wide bandwidth from 0.2 to 2.0 THz. Finally, we discuss the possible physical mechanism for the on-demand transparency of THz transmitted signals. Our work not only unveils critical experimental insights into electronic and optical properties of Dirac semimetal $PdTe_2$, but also provides practical applications of type II Dirac semimetals in photoactive THz photonics.

2. Results and Discussion

As shown in **Figure 1a**, $PdTe_2$ crystallizes in the CdI_2 (D^3_{3d}) structure with the P-3m1 space group formed by inserting a hexagonally packed layer of Pd atoms between every other layer of hexagonal close-packed Te atoms.[74–76] In this work, large-area $PdTe_2$ thin films (5 mm × 5 mm) were fabricated by the one-step pulsed laser deposition (PLD) technique without post annealing.[77–79]

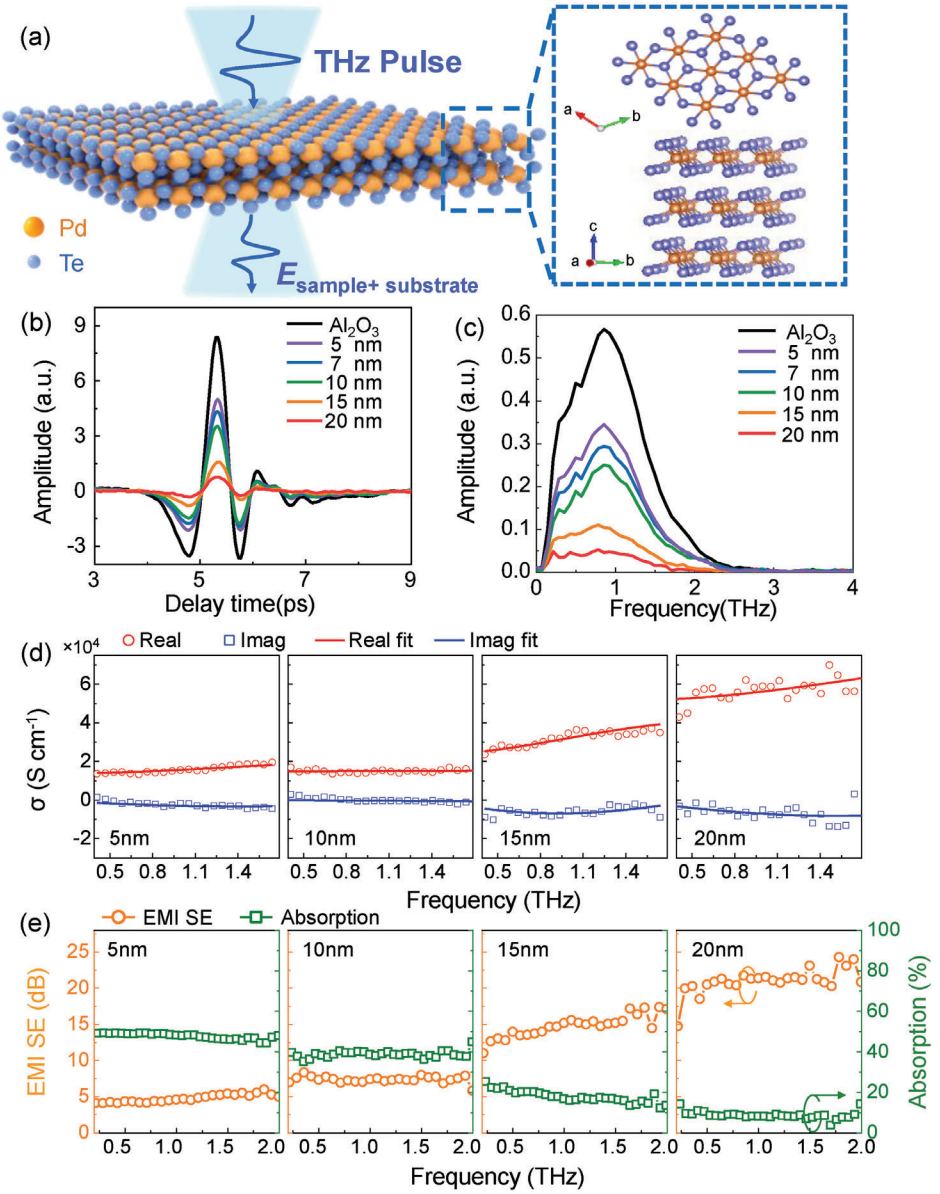

Figure 1. a) Schematic illustration of the THz-TDS spectroscopy on the semimetal $PdTe_2$ film. The enlarged images show the crystal structure of semimetal $PdTe_2$ at the *ab* and *bc* side views, respectively. b) Time-resolved THz electric field transmitted through the bare substrate and $PdTe_2$ films with different thicknesses grown on sapphire substrate. c) The THz signal transmitted in the frequency domain. d) The complex THz conductivity (red circles: real component; blue squares: imaginary component). The lines are Drude-Smith fits of the experimental data. e) THz EMI SE and THz absorption of $PdTe_2$ films with different thicknesses for ≈0.2–2.0 THz.

The as-grown films were characterized using atomic force microscopy (AFM), Raman microscopy and X-ray diffraction (XRD) to confirm the high quality and surface morphology (Sections S1 and S2, Supporting Information). The polycrystalline film is continuous over a large area. The conductivity of $PdTe_2$ thin films was investigated by broadband THz-TDS in a transmission configuration,[80,81] as depicted in Figure 1a, see Experimental Section.

Figure 1b shows the time-resolved THz electric field transmitted through $PdTe_2$ films grown on the sapphire substrate $E_{\text{sample + substrate}}(t)$ and through the bare substrate $E_{\text{substrate}}(t)$. We plot $E_{\text{sample + substrate}}(t)$ for different thicknesses of $PdTe_2$ films. It can be seen that the THz transmittance decreases as the thickness of the film increases. The corresponding frequency-domain spectra via Fourier transform of 5, 7, 10, 15, and 20 nm thick $PdTe_2$ are presented in Figure 1c. By comparing the amplitude and the phase of the THz pulses transmitted through the substrate and the $PdTe_2$ films on substrates, the complex THz conductivities $\tilde{\sigma}(\omega)$ of the semimetal $PdTe_2$ films are calculated by the Tinkham equation,[82,83]

$$\frac{\tilde{E}_{\text{sample + substrate}}(\omega)}{\tilde{E}_{\text{substrate}}(\omega)} = \frac{n+1}{n+1+Z_0\tilde{\sigma}(\omega)d} \quad (1)$$

where $Z_0 = 377\ \Omega$ is the impedance of the free space, $n = 3.07$ is the refractive index of the sapphire substrate in the THz frequency range (Section S3, Supporting Information) and d is the thickness of the $PdTe_2$ film. Figure 1d illustrates the real and imaginary parts of THz conductivity spectra for $PdTe_2$ films with thicknesses of 5, 10, 15, and 20 nm. It was observed that at low frequencies the real part of conductivity is suppressed, and that the imaginary part of conductivity is negative. The Drude–Smith model can be applied to the measured complex THz conductivity spectra[84,85]

$$\tilde{\sigma}(\omega) = \frac{\sigma_{DC}}{1 - i\omega\tau}\left(1 + \frac{c}{1 - i\omega\tau}\right) \quad (2)$$

where σ_{DC} is the DC conductivity, τ is the momentum scattering time. The DS model describes the backscattering or the localization of mobile charge transport in a disordered medium or the medium on a dielectric substrate. c is a phenomenological parameter, changing within the $-1 \le c \le 0$. $c = -1$ and 0 representing the carrier's momentum is completely backscattering over the short distances and fully randomized, respectively.[86,87] The experimental results can be fitted by the DS model very well. The charge transport parameters are summarized in Section S4 (Supporting Information). For a 20-nm-thick semimetal $PdTe_2$ film, $\sigma_{DC} \approx 5.68 \times 10^4$ S cm^{-1}, $\tau \approx 29.9$ fs, and $c \approx -0.65$ can be extracted, which indicate that the carriers are localized or coupled with the lattice deformations occurring collision events.[88] The intrinsic charge mobility μ depends on two quantities, effective mass m^* and scattering time τ, $\mu = \frac{e\tau}{m^*} \approx 175$ cm^2/(V · s), where e is the elementary charge and $m^* = 0.3\ m_e$ with m_e the rest electron mass.[39,67,89] Furthermore, the density of electron N can be calculated, $N = \frac{\sigma_{DC} m^*}{e^2 \tau} \approx 1.84 \times 10^{21}$ cm^{-3}.

Figure 1e shows the efficiency of THz EMI SE, owing to the high mobile carrier density and conductivity, defined as:[90,91]

$$\text{EMI SE} = -20 \log\left(\frac{E_{\text{sample + substrate}}(\omega)}{E_{\text{substrate}}(\omega)}\right) \quad (3)$$

The EMI SE of the semimetal $PdTe_2$ thin film increases with its thickness (Figure 1e; Section S5, Supporting Information). We find that EMI SE can reach up to ≈19.65 ± 4.80 dB (averaged over frequency range of 0.2–2.0 THz) for a 20-nm semimetal $PdTe_2$ film, which meets the requirement of THz EMI shielding materials. In order to more objectively evaluate the performance, the specific shielding efficiency ($\frac{\text{EMI SE}}{\text{thickness}}$) values for $PdTe_2$ films with different thicknesses can be used to compared with that of other THz EMI shielding materials, as shown in Table 1. Noted that the averaged $\frac{\text{EMI SE}}{\text{thickness}}$ of 20 nm-thick semimetal $PdTe_2$ film in this work can reach up to 982.50 ± 240.00 dB μm^{-1} over frequency range of 0.2–2.0 THz, which is better than the reported materials. The value is higher than 100 dB μm^{-1} of the MXene film[12] and 700 dB μm^{-1} of the MXene films with wrinkle microstructures.[19]

It should be noted that the measured THz EMI SE of conductive $PdTe_2$ films is the result of a combination of reflection and absorption losses experienced by the THz electromagnetic radiation. The absorption $A = 4g/(1 + 2g)^2$, where $g = R_{\square}/Z_0$, $R_{\square}$ is the square resistance of the film and Z_0 is the free space impedance of 377 Ω. According to the $R_{\square}$ of $PdTe_2$ films (Supplementary Section S6 and Figure S6, Supporting Information), we calculate the THz transmittance, reflection, and absorption of $PdTe_2$ films with different thicknesses (Section S6 and Figure S7, Supporting Information). The sheet resistance of 5-nm-thick sample is ≈126.72 ± 16.96 Ω sq^{-1}, which is closer to half of the free space resistance ($Z_0/2 = 188.5\ \Omega$ sq^{-1}). As shown in Figure 1e, the 5-nm-thick film has an average absorption of 47.80 ± 1.4% over the 0.2–2.0 THz range, approaching the theoretical absorption limit of 50%. As the thickness of the film increases from 5 to 20 nm, the average absorption gradually decreases from 47.80% ± 1.4% to 8.71% ± 1.9%, while the reflection increases from 36.07% ± 4.0% to 91.07% ± 2.0% in the broadband THz range. By optimization the thickness of the $PdTe_2$ improves the impedance matching of the thin film and finally approaches the maximum EMI SE in the broadband THz frequency range.

In the following, we carried out Optical-Pump THz-Probe (OPTP) measurements to examine the ultrafast manipulation of THz EMI SE by laser excitation, as shown in **Figure 2a**. In Figure 2b, it is worth comparing the typical dynamics of photoinduced THz peak amplitude transmittance ($-\Delta T/T_0$) through different materials, including Si, chemical vapor deposition (CVD)-grown doped graphene, Bi_2Se_3, $PdTe_2$ as a function of pump-to-probe time delay Δt. The $-\Delta T/T_0$ is related to the photoconductivity $\Delta\sigma = -\frac{1+n_{sub}}{Z_0 d}\frac{\Delta T}{T_0}$. Thus, the observed negative $\Delta T/T_0$ indicates an increase of the photoconductivity of the sample. Both sign and dynamics of the photoconductivity are determined by the photoinduced carriers' distribution in matters with different band structures, as shown in the inset of Figure 2b. A positive THz photoconductivity response with a very long lifetime is found in Si wafer, as the nature of its indirect band-gap.[92] Owing to the zero-band gap and linear energy-momentum characteristics at the Dirac point, the dynamical trace $\Delta\sigma(\Delta t)$ of CVD-grown graphene exhibits a sub-picosecond decrease followed by a several picoseconds mono-exponential decay.[93] In contrast, arising from the coexistence of Dirac-like surface states and the bulk band, the THz photoconductivity of topological insulator Bi_2Se_3 shows an initial rapid increase and then becomes negative, which can be attributed to the photocarriers transferred from the bulk state to the surface-state.[94,95] Notably, the transient THz photoconductivity in Dirac semimetal $PdTe_2$ film shows a distinctive feature. After photoexcitation, the 800 nm laser pulses enhance the transmission of the THz pulse propagating through the $PdTe_2$ film. The recover evolution exhibits a longer time scale on the order of hundreds of picoseconds.

Figure 2c shows the photo-modulation THz frequency-resolved ΔEMI SE measured at different delay times after photoexcitation. It can be seen that ΔEMI SE is negative, which means that the EMI SE is decreased over bandwidth of the THz radiation (0.2–2.0 THz). The suppression of EMI SE is a consequent result of the photo-induced decrease in the real part of the complex conductivity. For a fixed pump fluence of 0.85 mJ cm^{-2}, as the delay time Δt increased, the value of ΔEMI SE is gradually approaching to zero. For a fixed delay time at $\Delta t = 5$ ps, the negative ΔEMI SE increases with increasing pump fluence, as shown in Figure 2d. The maximum negative ΔEMI SE observed reaches −1.1 dB @ 2 THz at 1.13 mJ cm^{-2}, a value already exceeding three times that of ΔEMI SE ≈ −0.35 dB @ 2 THz measured on $Ti_3C_2T_y$ film with a pump fluence of 0.95 mJ cm^{-2}.[12]

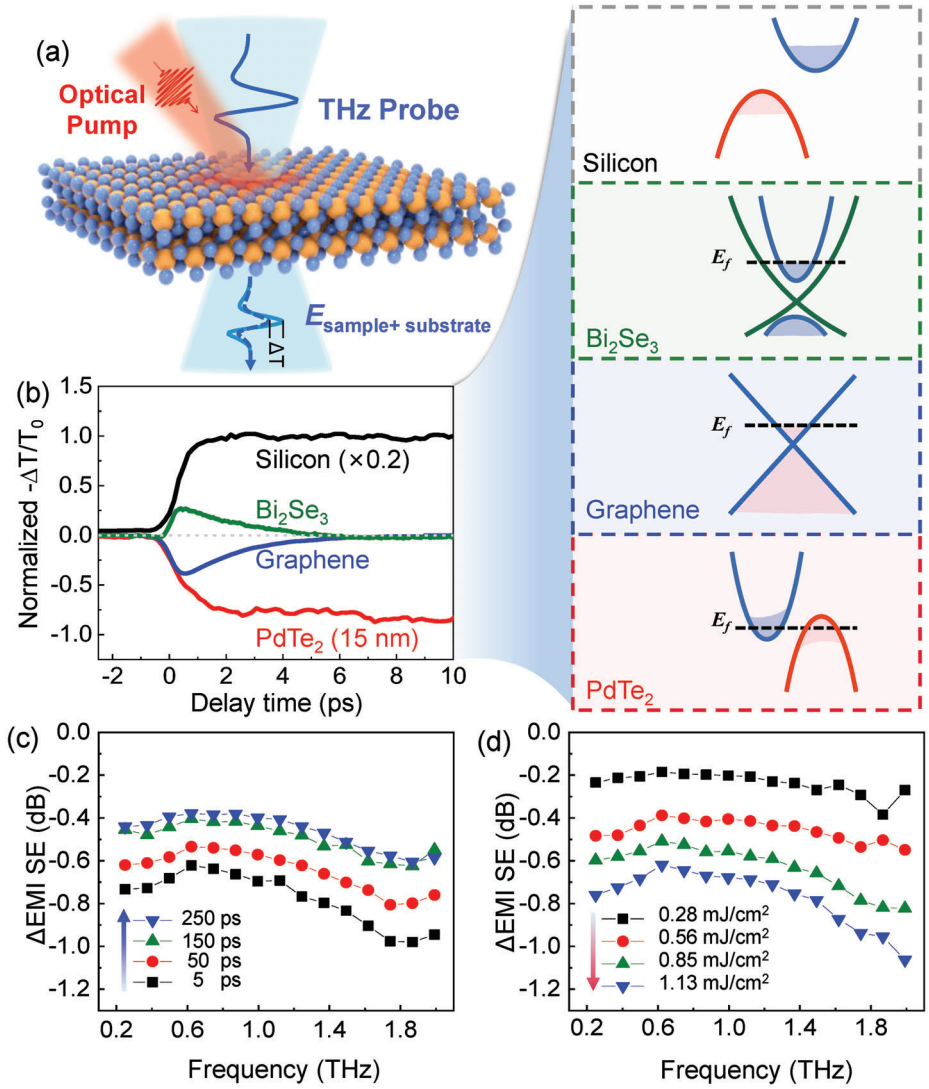

Figure 2. a) Schematic of the OPTP experiment for $PdTe_2$ films. b) The photo-modulation of transmitted THz peak electric field for Si, Bi_2Se_3, CVD-graphene, and $PdTe_2$ (15 nm). $\Delta T = T\text{-}T_0$ denotes the change of THz transmission, T and T_0 are defined as the THz peak amplitude in the presence and absence of optical pumping, respectively. The right inset: the band structure schematics of Si, Bi_2Se_3, CVD-graphene, and $PdTe_2$. c) Photoinduced changes in THz EMI SE at different delay times Δt excited with a pump fluence of 0.85 mJ cm^{-2}. d) Photoinduced changes in THz EMI SE at $\Delta t = 5$ ps excited with different pump fluences.

We now turn to the dynamics of the observed decrease of EMI SE and the transient increase in the THz pulse transmission under various pump fluences, as shown in **Figure 3**a. After the optical excitation, the photoinduced THz transmission rise gradually, and then decays over hundreds of picoseconds. As reported previously, the THz photoconductivity in type-II Dirac semimetal $PtTe_2$ shows an abrupt increase initially, and changes to negative in a sub-picosecond time scale, followed by a long recovery process that lasted a few nanoseconds.[88] Thus, we fit the experimental data to a biexponential decay function phenomenologically, including an absorption term, a bleaching decaying term and a constant term,

$$\frac{\Delta T(\Delta t)}{T_0} = H(t)\left[A\exp\left(-\frac{\Delta t}{\tau_1}\right) + B\exp\left(-\frac{\Delta t}{\tau_2}\right)\right] + C \quad (4)$$

where H(t) is the Heaviside step function, τ_1 and τ_2 are decay time constants, A and B are the corresponding amplitudes for photo-induced absorption and bleaching components. C represents the offset with long decay time, which cannot be accurately determined from the data. The fitting results are summarized in Figure 3d,e (Section S7, Supporting Information for details).

Taking the 15-nm $PdTe_2$ film as an example, the solid line in Figure 3b is fit of the experimental data using the Equation (4). The blue dotted cure shows the photo-induced absorption process, which consists of an initial rapid drop of $\Delta T(\Delta t)/T_0$ and a fast relaxation process with τ_1 of ≈0.92 ± 0.06 ps. The red dashed curve represents the photo-induced bleaching component, which consists of an initial rapid increase of $\Delta T(\Delta t)/T_0$ and a slow relaxation process with τ_2 of ≈529.45 ± 8.55 ps.

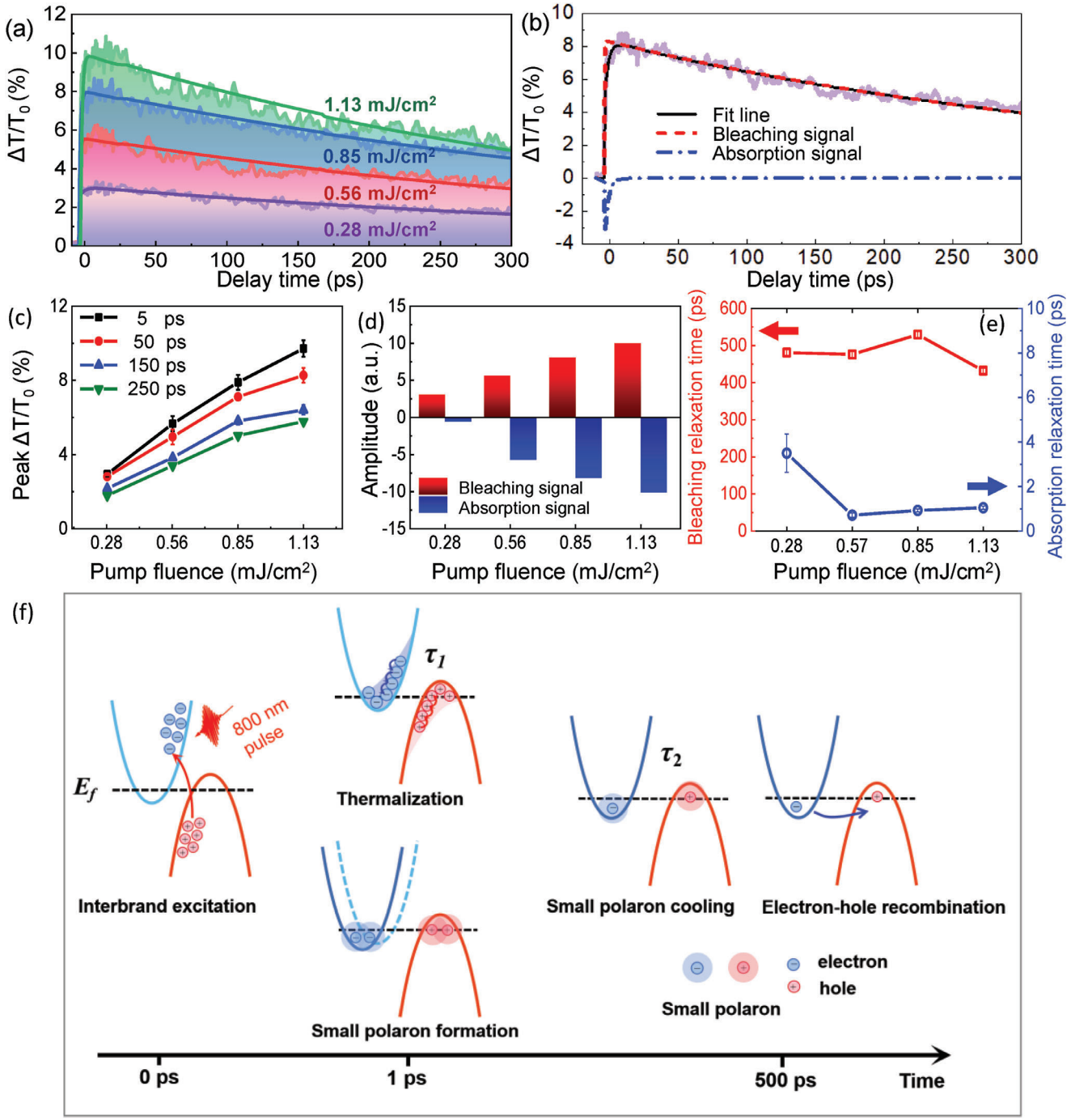

Figure 3. a) Photoinduced transient dynamics $\Delta T/T_0$ of 15-nm $PdTe_2$ films with different pump fluences, as a function of delay time Δt. b) $\Delta T/T_0$ (Δt) of 15-nm $PdTe_2$ with a pump fluence of 0.85 mJ cm^{-2}. The red and blue lines are the fitted curves for the biexponential decay function, representing the bleaching and absorption signals, respectively. c) The amplitudes of $\frac{\Delta T}{T_0}$ measured at four delay times as functions of pump fluences. d) Amplitudes of absorption and bleaching components fitted by Equation (4) with different pump fluences. e) Relaxation time of absorption and bleaching components as functions of pump fluences. f) Illustration of the photocarrier's relaxation process in type-II Dirac semimetal $PdTe_2$ film.

It can be found that the bleaching term (negative photoconductivity) dominates the overall transient THz transmission dynamics. The absorption term (positive photoconductivity) slows down the rising process of the photoinduced THz peak transmission.

The THz conductivity response of semimetal $PdTe_2$ to an ultrafast optical excitation is different from that of semiconductors. In semiconductors, the photoexcitation increases the carrier density in conduction band, and consequently, results in a positive photoconductivity.[96,97] In contrast, for the case of highly doped

or gated graphene, the redistribution of energy from photoexcited electron-hole pairs to initially unexcited free electrons, leading to heating either through direct conversion of excess energy into electronic heat or its dissipation into optical phonons.[98] The resulting reduction in conductivity recovers with a time constant of ≈2–6.8 ps, several orders of magnitude faster than that observed in $PdTe_2$. Note that, the pump-induced conductivity dynamics of Dirac semimetal $PdTe_2$ also shows a clear difference from that in Cd_3As_2. The positive THz photoconductivity of Cd_3As_2 relaxes through a single exponential decay with a time constant of ≈6.0 ps, which is dominated by the electron-hole recombination.[99] Since the semimetal film shows high carrier concentration, the formation of the exciton can be largely shielded by background free carriers. Thus, we ruled out the possibility of exciton formation in $PdTe_2$.[100] Furthermore, the THz generation from single-layer $PdTe_2$ is ≈500 times smaller than the transmitted THz pulse T_0. Therefore, the observed photomodulation of electromagnetic shielding effects in the $PdTe_2$ can rule out the contribution from the photoinduced THz emission.

Notably, $\Delta\sigma$ is determined by the photo-induced changes of carrier density (Δn) and carrier mobility ($\Delta\mu = \frac{e\Delta\tau}{m}$), $\Delta\sigma = \Delta n \times \mu \times e + n \times \Delta\mu \times e$, where e is elementary charge, $\Delta\tau$ is the photo-induced change of carrier scattering rate. After photoexcitation, the initial rapid photo-induced absorption (blue dashed line) is caused by the nonequilibrium carriers created by interband excitation, as shown in Figure 3f. The nonthermal carriers in the semimetal $PdTe_2$ will immediately thermalize within dozens of femtoseconds. During thermalization, the nonthermal carriers are scattered toward to the lowest conduction and valence bands, and ultimately all of them are converted into hot carriers with a statistical Fermi-Dirac distribution. Due to the strong and short-range electron-phonon (e-ph) coupling, the hot carriers would couple with the lattice vibrations of $PdTe_2$, forms small polarons. The small polaron formation leads to a significant reduction in carrier mobility due to the phonon "dressing" of carriers,[88] which results in the positive $\Delta T(\Delta t)/T_0$ signal. Therefore, the photoinduced absorption term corresponds to the hot electrons' behavior. While, the photoinduced bleaching term can be assigned to the photo-induced small polaron dynamics in the semimetal $PdTe_2$ film.

The formation of polarons after photoexcitation is further supported by the pump fluence dependent measurements. Figure 3c plots the $\Delta T(\Delta t)/T_0$ measured at delay times of Δt = 5, 50, 150, and 250 ps with respect to the pump fluence. The THz transmissions are almost linearly dependent on the optical pump fluence. Increasing the pump fluence induces a higher electron temperature in semimetal $PdTe_2$ film, more phonon modes can be excited during the hot carrier cooling process via *e*-ph coupling. Consequently, phonons can couple with more carriers at higher pump fluences, which causes the enhancement of THz transmission to be more pronounced. In Figure 3d, the amplitude of absorption and bleaching terms are comparable, increase almost linearly with the pump fluence. While, the time constant for photoinduced absorption process is ≈0.71–3.49 ps, which is much shorter compared to that of photoinduced bleaching term with hundreds of picoseconds, as shown in Figure 3e. Noted that, in contrast to the previously reported $PtTe_2$, $PdTe_2$ displays dominating negative photoconductivity signals. According to the fitting results, the thermalization of photocarriers occurs simultaneously with the process of formation of small polarons due to *e*-ph coupling, while the formation of small polarons dominates. This demonstrates that $PdTe_2$ has a stronger e-ph coupling strength.[42] The photoinduced small polaron is composed of hot photoinduced carrier and cold lattice. The hundreds of picoseconds can be assigned to the polaron cooling process occurring via transferring the excess energy to the deformed lattice and electron-hole recombination, as shown in Figure 3f.

In order to further shed more light on applications, we have carried out thickness dependent measurements with same optical excitation fluence at room temperature. **Figure 4a** shows the photoinduced $\Delta T(\Delta t)/T_0$ for 5, 7, 10, 15, and 20 nm, which are fitted by Equation (4). As shown in Figure 4b, when the thickness increases from 5 to 15 nm, the positive $\Delta T(\Delta t)/T_0$ increase from 2.0% to 8.4%, and then decreases to 3.7% for the 20 nm thick sample, which is consistent with that found in $PtTe_2$.[88] The extracted τ_2 varies from ≈249.7 ± 3.9 ps for 5 nm sample to ~407.0 ± 6.3 ps for 15 nm sample, and up to ≈2437.8 ± 182.1 ps for 20 nm sample (Section S8, Supporting Information for details). It is noticeable that the longer relaxation time observed in the thicker film, which demonstrates that polaron dissociation process becomes slower in the thicker film with stronger e-ph coupling. The thicker film has better crystalline as supported by the Raman and XRD results. More defects are present in the thinner film, which accelerates charge carrier recombination in semimetal $PdTe_2$.

Figure 4c shows the photoinduced negative THz conductivity spectra in the frequency range of 0.2–2.0 THz at pump-probe delay time of 5 ps. $\Delta\sigma(\omega)$ is fitted by a DS model characterizing the local properties of the carriers $\Delta\sigma_{DC} \approx 4.69 \times 10^2$ S cm^{-1} (Section S9, Supporting Information for details). Different from the intrinsic THz conductivity dispersion mentioned above, the pump-induced conductivity spectra do not coincide with the DS model exactly, indicating the feature of strong localization of photocarriers after photoexcitation, which further confirms small polaron formation in $PdTe_2$ film.

As mentioned above, the THz photoconductivity dynamics can be modulated via e-ph coupling by changing the thickness of $PdTe_2$ films. Accordingly, the dynamics of $\Delta T(\Delta t)/T_0$ for different thickness samples can further be used to modulate the photoinduced ΔEMI SE. In order to clearly compare the photoinduced ΔEMI SE of the semimetal $PdTe_2$, Figure 4d,e shows the ΔEMI SE for 5, 7, 10, and 15 nm films measured at delay times of 5 and 150 ps, respectively. It can be found that photoinduced ΔEMI SE at Δt = 5 ps change from −0.70 dB @ 15 nm, − 0.43 dB @ 10 nm, −0.26 dB @7 nm to −0.19 dB @ 5 nm measured at 1.0 THz. While, for Δt = 150 ps, the ΔEMI SE decreases to be −0.44 dB @ 15 nm, − 0.31 dB @ 10 nm, −0.16 dB @ 7 nm, and −0.09 dB @ 5 nm measured at 1.0 THz.

3. Conclusion

In conclusion, we have fabricated the large-area $PdTe_2$ thin films on sapphire substrates by the PLD. We have applied a combination of THz TDS and OPTP measurements to investigate the optoelectronic properties of $PdTe_2$ thin films. It has been demonstrated that $PdTe_2$ films have high THz conductivity and exhibit highly efficient EMI shielding properties in the THz range.

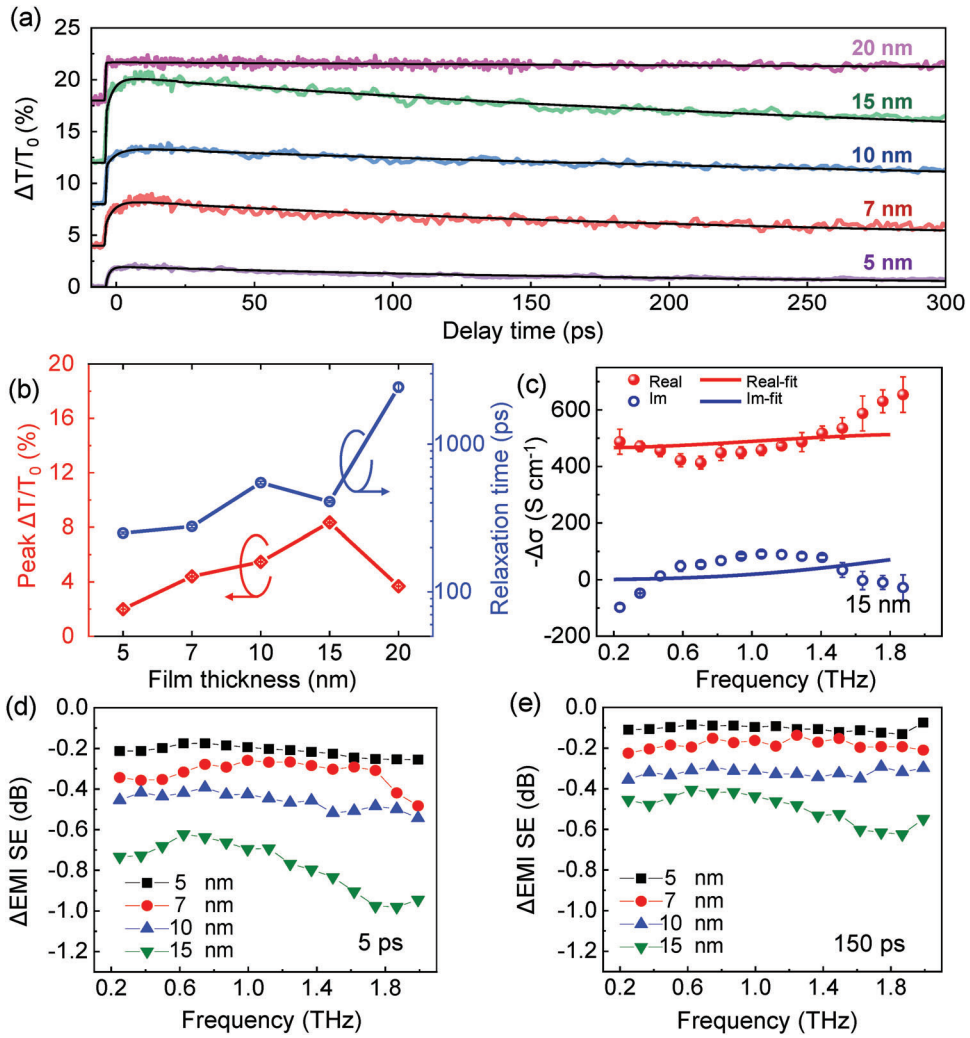

Figure 4. a) The photoinduced transient THz transmission of the $PdTe_2$ with different thicknesses, using excitation of 800 nm and a pump fluence of 0.85 mJ cm^{-2}. The $\Delta T(t)/T_0$ are shifted on the *y*-axis for clarity. b) Peak values of $\Delta T(t)/T_0$ and relaxation times of bleaching components as a function of film thickness. c) Photo-induced THz complex conductivity and the DS model fit of 15 nm $PdTe_2$. The red circles: real part of the THz photoconductivity, the blue circles: imaginary part of the THz photoconductivity, the solid lines: DS model fit. The thickness dependences of the ΔEMI SE for two delay times of d) 5 ps and e) 150 ps.

Their shielding efficiency can be reduced on demand for hundred picoseconds-long time scale by ultrashort optical pulses. The functionality is dependent on the pump fluence and the film thickness. Our findings make $PdTe_2$ a promising material for THz EMI shielding where the dynamical control over the SE is required, which would open on-demand THz communication channels. The optically gated THz transparency may be required for sensitive THz detectors. The $PdTe_2$ thin films further add to attractiveness of this emergent class of Dirac semimetals for the practical applications in THz technology and EMI shielding applications.

4. Experimental Section

Fabrication of $PdTe_2$ Films: The large-area $PdTe_2$ films (5 mm × 5 mm) were fabricated by the one-step pulsed laser deposition technique without post annealing. It has the advantages of better flatness, high deposition rates, and relatively low growth temperatures, all of these make it well applicable for depositing 2D materials. In addition, the thickness of the films can be controlled by changing the number of laser pulses. The target was prepared by heating mixed palladium (99.99%) and tellurium (99.99%) powders with a stoichiometric ratio of 1:2.5 at 950 °C for a week. The basic pressure of the PLD vacuum chamber was ≈2.9×10^{-7} mbar, and the distance between the substrate and target was ≈5 cm. The sapphire substrate with the size of 5 × 5 mm^2 was heated to 200 °C at a speed of 2 °C min^{-1}. The large-area $PdTe_2$ film was deposited onto the sapphire substrate at a speed of 0.16 nm min^{-1} by using a 248-nm KrF excimer laser beam with an average fluence of 1 J cm^{-2} and a repetition rate of 1 Hz. The as-grown films were characterized using atomic force microscopy, Raman microscopy, and X-ray diffraction to confirm the high quality of the films (See Sections S1 and S2, Supporting Information for details). Two pronounced phonon modes at 75.53 cm^{-1} (E_g) and 132.51 cm^{-1} (A_{1g}) are observed for all films, which correspond to the in-plane and out-of-plane Te atom vibration modes, respectively. The film deposited on the sapphire substrate is continuous and uniform, without any cracks and ripples.

THz Time-Domain Spectroscopy (THz TDS): A standard ZnTe crystal-based THz TDS was used to measure the THz transmission spectrum. THz TDS is a contactless experimental technique that enables determination of the complex optical conductivity of an electronic material without involving the Kramers–Kronig transformation.[80] The femtosecond laser pulse (central wavelength 800 nm, repetition frequency 1 kHz, pulse width 120 fs) was split into two beams. The generation beam was modulated by an optical chopper and focused on a 1 mm thick <110> ZnTe crystal. The emitted THz beam was focused by parabolic mirrors and transmitted through the $PdTe_2$ films grown on sapphire substrates. The detection laser beam was used to record the THz waveform coherently by free space electrooptical sampling in a 1 mm thick <110> ZnTe crystal. The temporal THz fields transmitted through the $PdTe_2$ films on the sapphire substrate were recorded by using a scanning delay line. The sampling window is 14 ps, which offers the frequency resolution of 0.0714 THz.

Optical-Pump THz-Probe Spectroscopy (OPTP): The photo-induced carrier dynamics of the $PdTe_2$ films were investigated by OPTP spectroscopy, in a traditional normal-incidence transmission configuration. The THz generation and detection have been mentioned above. For the optical excitation, linearly polarized 120 fs laser pulse was used with central wavelength of 800 nm. The laser pulse illuminates on the sample at normal incidence with a beam diameter of ≈5 mm, which was larger than the focused THz beam spot size of ≈3 mm in diameter at the sample point, for homogenous photoexcitation. Details of the OPTP setup can be found in Ref. [81]. By using OPTP setup, the ultrafast optoelectronic properties of semimetal $PdTe_2$ films can be measured. The THz pulse measures the electronic transitions around the Fermi level of sample. All measurements were performed at room temperature and were purged with dry air to avoid water vapor absorption. No obvious photodegradation or thermal damage was found during a 12 h experimental period.

Supporting Information

Supporting Information is available from the Wiley Online Library or from the author.

Acknowledgements

Y.G. and Z.C. contributed equally to this work. This work was supported by the National Key Research and Development Program of China (2023YFF0719200, 2022YFA1404004), National Natural Science Foundation of China (62322115, 61988102, 61975110, 62335012), 111 Project (D18014); the Key project supported by Science and Technology Commission Shanghai Municipality (YDZX20193100004960); Science and Technology Commission of Shanghai Municipality (22JC1400200, 21S31907400); X.W is grateful to the financial supporting from the National Key Research and Development Program of China (Grant No. 2022YFA1402404), the National Natural Science Foundation of China (Grant nos. T2394473 and 62274085) and Fundamental Research Funds for the Central Universities (021014380225).

Conflict of Interest

The authors declare no conflict of interest.

Data Availability Statement

The data that support the findings of this study are available from the corresponding author upon reasonable request.

Keywords

dirac semimetal, small polaron, terahertz electromagnetic interference shielding, ultrafast carrier dynamics

Received: May 7, 2024
Revised: June 22, 2024
Published online:

[1] X. Zhang, A. Shkurinov, Y. Zhang, *Nat. Photon.* **2017**, *11*, 16.
[2] T. L. Cocker, V. Jelic, R. Hillenbrand, F. A. Hegmann, *Nat. Photon.* **2021**, *15*, 558.
[3] M. Tonouchi, *Nat. Photon.* **2007**, *1*, 97.
[4] K. Sengupta, T. Nagatsuma, D. M. Mittleman, *Nat. Electron.* **2018**, *1*, 622.
[5] T. Nagatsuma, G. Ducournau, C. Renaud, *Nat. Photon.* **2016**, *10*, 371.
[6] T. Kampfrath, K. Tanaka, K. A. Nelson, *Nat. Photon.* **2013**, *7*, 680.
[7] M. Koch, D. M. Mittleman, J. Ornik, E. Castro-Camus, *Nat. Rev. Methods Primers.* **2023**, *3*, 48.
[8] X. Li, J. Li, Y. Li, A. Ozcan, M. Jarrahi, *Light Sci Appl.* **2023**, *12*, 233.
[9] K. Tian, D. Hu, Q. Wei, Q. Fu, H. Deng, *J. Mater. Sci. Technol.* **2023**, *134*, 106.
[10] A. Iqbal, P. Sambyal, C. M. Koo, *Adv. Funct. Mater.* **2020**, *30*, 2000883.
[11] M. Alhabeb, K. Maleski, B. Anasori, P. Lelyukh, L. Clark, S. Sin, Y. Gogotsi, *Chem. Mater.* **2017**, *29*, 7633.
[12] G. Li, N. Amer, H. A. Hafez, S. Huang, D. Turchinovich, V. N. Mochain, F. A. Hegmann, L. V. Titova, *Nano Lett.* **2020**, *20*, 636.
[13] Z. Lin, J. Liu, W. Peng, Y. Zhu, Y. Zhao, K. Jiang, M. Peng, Y. Tan, *ACS Nano.* **2020**, *14*, 2109.
[14] H. Wan, N. Liu, J. Tang, Q. Wen, X. Xiao, *ACS Nano.* **2021**, *15*, 13646.
[15] Z. Cheng, Y. Cao, R. Wang, X. Liu, F. Fan, Y. Huang, *J. Mater. Chem. A.* **2023**, *11*, 5593.
[16] V. C. S. Theja, D. S. Assi, H. Huang, R. S. Alsulami, B. Chen, C. Chan, C. Shek, V. Karthikeyan, V. A. L. Roy, *Adv. Mater. Interfaces.* **2023**, *10*, 2300440.
[17] S. Li, S. Xu, K. Pan, J. Du, J. Qiu, *Carbon.* **2022**, *194*, 127.
[18] S. Yang, R. Yang, Z. Lin, X. Wang, S. Liu, W. Huang, Z. Chen, J. Wei, Z. Zeng, H. Chen, Y. Hu, X. Gui, *J. Mater. Chem. C.* **2022**, *10*, 14929.
[19] S. Yang, Z. Lin, X. Wang, J. Huang, R. Yang, Z. Chen, Y. Jia, Z. Zeng, Z. Cao, H. Zhu, Y. Hu, E. Li, H. Chen, T. Wang, S. Deng, X. Gui, *Nano-Micro Lett.* **2024**, *16*, 165.
[20] Z. Huang, H. Chen, S. Xu, L. Chen, Y. Huang, Z. Ge, W. Ma, J. Liang, F. Fan, S. Chang, Y. Chen, *Adv. Opt. Mater.* **2018**, *6*, 1801165.
[21] S. Hou, W. Ma, G. Li, Y. Zhang, Y. Ji, F. Fan, Y. Huang, *J. Mater. Sci. Technol.* **2020**, *52*, 136.
[22] C. Pavlou, M. G. P. Carbone, A. C. Manikas, G. Trakakis, C. Koral, G. Papari, A. Andreone, C. Galiotis, *Nat. Commun.* **2021**, *12*, 4655.
[23] S. Mukherjee, N. M. A. Kumar, B. Karthikeyan, N. Kamaraju, *Appl. Phys. A.* **2023**, *129*, 343.
[24] S. Venkatachalam, D. Bertin, G. Ducournau, J. F. Lampin, D. Hourlier, *Carbon.* **2016**, *100*, 158.
[25] G. Kulkarni, S. Rane, N. Acharyya, S. Patil, D. R. Chowdhury, V. Puri, *Ceram. Int.* **2023**, *49*, 39441.
[26] N. Arooj, M. Mumtaz, A. Rehman, I. Ahmad, S. Khan, A. Shah, M. ul Hassan, M. Raffi, *J. Appl. Polym.* **2023**, *140*, e53790.
[27] S. Park, J. Bang, B. S. Kim, S. J. Oh, J. H. Choi, *Mater. Today Adv.* **2021**, *12*, 100177.
[28] F. Shahzad, M. Alhabeb, C. B. Hatter, B. Anasori, S. M. Hong, C. M. Koo, Y. Gogotsi, *Science.* **2016**, *353*, 1137.
[29] Z. Chen, S. Yang, J. Huang, Y. Gu, W. Huang, S. Liu, Z. Lin, Z. Zeng, Y. Hu, Z. Chen, B. Yang, X. Gui, *Nano-Micro Lett.* **2024**, *16*, 92.
[30] K. F. Mak, J. Shan, *Nat. Photon.* **2016**, *10*, 216.
[31] C. Gong, Y. Zhang, W. Chen, J. Chu, T. Lei, J. Pu, L. Dai, C. Wu, Y. Cheng, T. Zhai, L. Li, J. Xiong, *Adv. Sci.* **2017**, *4*, 1700231.
[32] H. Wang, C. Li, P. Fang, Z. Zhang, J. Zhang, *Chem. Soc. Rev.* **2018**, *47*, 6101.

[33] S. Manzeli, D. Ovchinnikov, D. Pasquier, O. V. Yazyev, A. Kis, *Nat. Rev. Mater.* **2017**, *2*, 17033.
[34] S. E. Muller, M. P. Prange, Z. Lu, W. S. Rosenthal, J. A. Bilbrey, *Sci. Data.* **2023**, *10*, 336.
[35] K. F. Mak, D. Xiao, J. Shan, *Nat. Photon.* **2018**, *12*, 451.
[36] H. J. Noh, J. Jeong, E. J. Cho, K. Kim, B. I. Min, B. G. Park, *Phys. Rev. Lett.* **2017**, *119*, 016401.
[37] A. Sirohi, S. Das, P. Adhikary, R. R. Chowdhury, A. Vashist, Y. Singh, S. Gayen, T. Das, G. Sheet, *J. Phys.: Condens. Matter.* **2019**, *31*, 085701.
[38] Y. liu, J. Zhao, L. Yu, C. Lin, A. Liang, C. Hu, Y. Ding, Y. Xu, S. He, L. Zhao, G. Liu, X. Dong, J. Zhang, C. Chen, Z. Xu, H. Weng, X. Dai, Z. Fang, X. Zhou, *Chin. Phys. Lett.* **2015**, *32*, 067303.
[39] H. Leng, C. Paulsen, Y. Huang, A. de Visser, *Phys. Rev. B.* **2017**, *96*, 220506.
[40] F. Fei, X. Bo, R. Wang, B. Wu, J. Jiang, D. Fu, M. Gao, H. Zheng, Y. Chen, X. Wang, H. Bu, F. Song, X. Wan, B. Wang, G. Wang, *Phys. Rev. B.* **2017**, *96*, 041201.
[41] J. Cook, S. Mardanya, Q. Lu, C. Conner, M. Snyder, X. Zhang, J. McMillen, G. Watson, T. Chang, G. Bian, *Nano Lett.* **2023**, *23*, 1752.
[42] R. K. S. Amit, N. Wadehra, S. Chakraverty, Y. Singh, *Phys Rev.* **2018**, *2*, 114202.
[43] L. Li, Z. Huang, J. Xu, H. Huang, *Front Chem.* **2022**, *10*, 1061703.
[44] S. Liu, S. Zhu, Q. Wu, C. Zhang, P. Song, Y. Shi, H. Liu, Z. Liu, J. Song, F. Wu, Y. Zhao, X. Tang, Y. Yuan, H. Huang, J. He, H. Liu, Y. Duan, J. Meng, *Results Phys.* **2021**, *30*, 104816.
[45] G. Anemone, P. C. Aguilar, M. Garnica, F. Calleja, A. Al Taleb, C. Kuo, C. Lue, A. Politano, A. L. V. de Parga, G. Benedek, D. Farías, R. Miranda, *NPJ 2D Mater Appl.* **2021**, *5*, 25.
[46] J. Meng, H. Xue, M. Liu, W. Jiang, Z. Zhang, J. Ling, L. He, R. Dou, C. Xiang, J. Nie, *J. Phys.: Condens. Matter.* **2020**, *32*, 015702.
[47] B. Marfoua, J. Hong, *ACS Appl. Mater. Interfaces.* **2019**, *11*, 38819.
[48] G. D'Olimpio, C. Guo, C. N. Kuo, R. Edla, C. S. Lue, L. Ottaviano, P. Torelli, L. Wang, D. W. Boukhvalov, A. Politano, *Adv. Funct. Mater.* **2020**, *30*, 1906556.
[49] J. Guo, Y. Zhang, S. Yue, C. Li, Z. Wang, *J. Phys. Chem. Solids.* **2023**, *181*, 111531.
[50] P. Cheng, S. Ahmed, J. Qiao, L. W. Wong, C. Yuen, A. M. Saleque, M. N. A. Ivan, S. U. Hani, M. I. Hossain, J. Zhao, Q. Wen, Y. Tsang, *Appl. Mater. Today.* **2022**, *26*, 101296.
[51] H. Lu, J. He, Z. Hu, X. Hu, P. He, Y. Zhao, M. Hao, L. Tao, *Infrared Phys. Technol.* **2021**, *119*, 103962.
[52] Y. Qu, C. T. Kwok, Y. Shao, X. Shi, Y. Kawazoe, H. Pan, *Int. J. Hydrog. Energy.* **2021**, *46*, 9371.
[53] C. Guo, Y. Hu, G. Chen, D. Wei, L. Zhang, Z. Chen, W. Guo, H. Xu, C. N. Kuo, C. Lue, X. Bo, X. Wan, L. Wang, A. Politano, X. Chen, W. Lu, *Sci. Adv.* **2020**, *6*, eabb6500.
[54] L. Zhang, C. Guo, C. N. Kuo, H. Xu, K. Zhang, B. Ghosh, J. De Santis, D. W. Boukhvalov, I. Vobornik, V. Paolucci, C. Lue, H. Xing, A. Agarwal, L. Wang, A. Politano, *Phys. Status Solidi RRL.* **2021**, *15*, 2100212.
[55] Y. Peng, J. Huang, J. Luo, Z. Yang, L. Wang, X. Wu, X. Zang, C. Yu, M. Gu, Q. Hu, X. Zhang, Y. Zhu, S. Zhuang, *PhotoniX.* **2021**, *2*, 12.
[56] Z. Dong, W. Yu, L. Zhang, L. Yang, L. Huang, Y. Zhang, Z. Ren, H. Mu, C. Chen, J. Zhang, J. Li, L. Wang, K. Zhang, *InfoMat.* **2023**, *5*, e12403.
[57] R. B. Schulz, V. C. Plantz, D. R. Brush, *IEEE Trans. Electromagn. Compat.* **1988**, *30*, 187.
[58] J. Zheng, T. Miao, R. Xu, X. Ping, Y. Wu, Z. Lu, Z. Zhang, D. Hu, L. Liu, Q. Zhang, D. Li, Z. Cheng, W. Ma, L. Xie, L. Jiao, *Adv. Mater.* **2021**, *33*, 2101150.
[59] T. Miao, M. Xiang, D. Li, X. Wang, *Nanoscale.* **2022**, *14*, 10101.
[60] C. Zhang, S. Peng, J. Han, C. Li, H. Zhou, H. Yu, J. Gou, C. Chen, Y. Jiang, J. Wang, *Adv. Funct. Mater.* **2023**, *33*, 2302466.
[61] N. van Hoof, M. Parente, A. Baldi, J. G. Rivas, *Adv. Opt. Mater.* **2020**, *8*, 1900790.
[62] T. Zhao, P. Xie, H. Wan, T. Ding, M. Liu, J. Xie, E. Li, X. Chen, T. Wang, Q. Zhang, Y. Wei, Y. Gong, Q. Wen, M. Hu, C. Qiu, X. Xiao, *Nat. Photon.* **2023**, *17*, 622.
[63] C. Pavlou, M. G. P. Carbone, A. C. Manikas, G. Trakakis, C. Koral, G. Papari, A. Andreone, C. Galiotis, *Nat. Commun.* **2021**, *12*, 4655.
[64] A. Iqbal, F. Shahzad, K. Hantanasirisakul, M. K. Kim, J. Kwon, J. Hong, H. Kim, D. Kim, Y. Gogotsi, C. M. Koo, *Science.* **2020**, *369*, 446.
[65] X. Wang, S. Liao, Y. Wan, P. Zhu, Y. Hu, T. Zhao, R. Sun, C. Wong, *J. Mater. Chem. C.* **2022**, *10*, 44.
[66] Y. Liu, Y. Wang, N. Wu, M. Han, W. Liu, J. Liu, Z. Zeng, *Nano-Micro Lett.* **2023**, *15*, 240.
[67] Y. Peng, C. Shi, Y. Zhu, M. Gu, S. Zhuang, *PhotoniX.* **2020**, *1*, 12.
[68] Y. Zhu, X. Zang, H. Chi, Y. Zhou, Y. Zhu, S. Zhuang, *Light: Adv. Manufact.* **2023**, *4*, 2689.
[69] X. Zang, B. Yao, L. Chen, J. Xie, X. Guo, A. V. Balakin, A. P. Shkurinov, S. Zhuang, *Light: Adv. Manufact.* **2021**, *2*, 10.
[70] J. Lyu, S. Shen, L. Chen, Y. Zhu, S. Zhuang, *PhotoniX.* **2023**, *4*, 28.
[71] Z. Chen, H. Qiu, X. Cheng, J. Cui, Z. Jin, D. Tian, X. Zhang, K. Xu, R. Liu, W. Niu, L. Zhou, T. Qiu, Y. Chen, C. Zhang, X. Xi, F. Song, R. Yu, X. Zhai, B. Jin, R. Zhang, X. Wang, *Nat. Commun.* **2024**, *15*, 2605.
[72] Z. Dai, M. Manjappa, Y. Yang, T. C. W. Tan, B. Qiang, S. Han, L. Wong, F. Xiu, W. Liu, R. Singh, *Adv. Funct. Mater.* **2021**, *31*, 2011011.
[73] Y. Li, W. Yu, K. Zhang, N. Cui, T. Yun, X. Xia, Y. Jiang, G. Zhang, H. Mu, S. Lin, *Mater. Horiz.* **2024**, *11*, 2572.
[74] A. E. Dunsworth, *J. Low Temp. Phys.* **1975**, *19*, 51.
[75] G. W. Ryan, W. L. Sheils, *Phys. Rev. B.* **2000**, *61*, 8526.
[76] Y. Wang, J. Zhang, W. Zhu, Y. Zou, C. Xi, L. Ma, T. Han, J. Yang, J. Wang, J. Xu, L. Zhang, L. Pi, C. Zhang, Y. Zhang, *Sci. Rep.* **2016**, *6*, 31554.
[77] W. Zhuang, Z. Chen, X. Wang, *Adv Phys X.* **2022**, *7*, 2034529.
[78] Y. Chen, Y. Zhu, R. Lin, W. Niu, R. Liu, W. Zhuang, X. Zhang, J. Liang, W. Sun, Z. Chen, Y. Hu, F. Song, J. Zhou, D. Wu, B. Ge, H. Yang, R. Zhang, X. Wang, *Adv. Funct. Mater.* **2023**, *33*, 2302984.
[79] B. Wang, Z. Zhang, S. Zhong, Z. Zheng, P. Xu, H. Zhang, *J. Mater. Chem. C.* **2020**, *8*, 4988.
[80] J. E. Bertie, Z. Lan, *J. Chem. Phys.* **1996**, *105*, 8502.
[81] Z. Jin, Y. Peng, Y. Fang, Z. Ye, Z. Fan, Z. Liu, X. Bao, H. Gao, W. Ren, J. Wu, G. Ma, Q. Chen, C. Zhang, A. V. Balakin, A. P. Shkurinov, Y. Zhu, S. Zhuang, *Light Sci Appl.* **2022**, *11*, 209.
[82] R. Ulbricht, E. Hendry, J. Shan, T. F. Heinz, M. Bonn, *Rev. Mod. Phys.* **2017**, *83*, 029901.
[83] Z. Jin, D. Gehrig, C. Dyer-Smith, E. J. Heilweil, F. Laquai, M. Bonn, D. Turchinovich, *J. Phys. Chem. Lett.* **2014**, *5*, 3662.
[84] N. V. Smith, *Phys. Rev. B.* **2001**, *64*, 155106.
[85] T. L. Cocker, D. Baillie, M. Buruma, L. V. Titova, R. D. Sydora, F. Marsiglio, F. A. Hegmann, *Phys. Rev. B.* **2017**, *96*, 205439.
[86] Z. Jin, S. Ruan, X. Zhou, B. Song, C. Song, X. Chen, F. Pan, Y. Peng, C. Zhang, G. Ma, Y. Zhu, S. Zhuang, *Phys. Rev. B.* **2020**, *102*, 014438.
[87] X. Xing, Z. Zhang, G. Ma, *Photonics.* **2023**, *10*, 810.
[88] P. Suo, H. Zhang, S. Yan, W. Zhang, J. Fu, X. Lin, S. Hao, Z. Jin, Y. Zhang, C. Zhang, F. Miao, S. Liang, G. Ma, *Phys. Rev. Lett.* **2021**, *126*, 227402.
[89] M. V. Salis, P. Rodière, H. Leng, K. Huang, A. de Visser, *J. Phys.: Condens. Matter.* **2018**, *30*, 505602.
[90] L. Liu, A. Das, C. M. Megaridis, *Carbon.* **2014**, *69*, 1.
[91] R. Kumar, S. Sahoo, E. Joanni, J. J. Shim, *Compos. Part. B-Eng.* **2023**, *264*, 110874.
[92] G. Li, D. Li, Z. Jin, G. Ma, *Opt. Commun.* **2012**, *285*, 4102.

[93] C. J. Docherty, C. T. Lin, H. J. Joyce, R. J. Nicholas, L. M. Herz, L. Li, M. B. Johnston, *Nat. Commun.* **2012**, *3*, 1228.
[94] J. Zhou, T. Zhou, D. Yang, Z. Wang, Z. Zhang, J. You, Z. Xu, X. Zheng, X. Cheng, *Photonic Sens.* **2019**, *9*, 268.
[95] W. Wang, K. Sun, C. Wang, W. Zhang, P. Suo, X. Lin, G. Ma, *J. Phys. Chem. C.* **2023**, *127*, 23778.
[96] J. Lloyd-Hughes, T. I. Jeon, *J. Infrared Milli. Terahz. Waves.* **2012**, *33*, 871.
[97] J. Fu, W. Xu, X. Chen, S. Zhang, W. Zhang, P. Suo, X. Lin, J. Wang, Z. Jin, W. Liu, G. Ma, *J. Phys. Chem. C.* **2020**, *124*, 10719.
[98] Z. Zhang, T. Lin, X. Xing, X. Lin, X. Meng, Z. Cheng, Z. Jin, G. Ma, *Appl. Phys. Lett.* **2017**, *110*, 111108.
[99] W. Zhang, Y. Yang, P. Suo, W. Zhao, J. Guo, Q. Lu, X. Lin, Z. Jin, L. Wang, G. Chen, F. Xiu, W. Liu, C. Zhang, G. Ma, *Appl. Phys. Lett.* **2019**, *114*, 221102.
[100] C. H. Lui, A. J. Frenzel, D. V. Pilon, Y. Lee, X. Ling, G. M. Akselrod, J. Kong, N. Gedik, *Phys. Rev. Lett.* **2014**, *113*, 166801.